



HAL
open science

Experimental insights into the interplay between buoyancy, convection and dissolution reaction

A. Ahoulou, A.-J. Tinet, C. Oltéan, F. Golfier

► **To cite this version:**

A. Ahoulou, A.-J. Tinet, C. Oltéan, F. Golfier. Experimental insights into the interplay between buoyancy, convection and dissolution reaction. *Journal of Geophysical Research: Solid Earth*, 2020, 1125 (11), 10.1029/2020JB020854 . hal-02981568

HAL Id: hal-02981568

<https://hal.science/hal-02981568>

Submitted on 25 Jun 2022

HAL is a multi-disciplinary open access archive for the deposit and dissemination of scientific research documents, whether they are published or not. The documents may come from teaching and research institutions in France or abroad, or from public or private research centers.

L'archive ouverte pluridisciplinaire **HAL**, est destinée au dépôt et à la diffusion de documents scientifiques de niveau recherche, publiés ou non, émanant des établissements d'enseignement et de recherche français ou étrangers, des laboratoires publics ou privés.

Copyright

JGR Solid Earth

RESEARCH ARTICLE

10.1029/2020JB020854

Key Points:

- Use of a laboratory physical model and morphological descriptors to study the influence of density contrast on dissolution regimes
- No additional pattern was observed but displacement of transition between patterns toward higher Péclet/lower Damköhler induced by buoyancy
- A modification of interface morphology, with larger roughness, has been highlighted for high Richardson number

Correspondence to:

A. W. A. Ahoulou,
assohoun-wilfried.ahoulou@univ-lorraine.fr

Citation:

Ahoulou, A. W. A., Tinet, A.-J., Oltéan, C., & Golfier, F. (2020). Experimental insights into the interplay between buoyancy, convection, and dissolution reaction. *Journal of Geophysical Research: Solid Earth*, 125, e2020JB020854. <https://doi.org/10.1029/2020JB020854>

Received 25 AUG 2020

Accepted 20 OCT 2020

Accepted article online 22 OCT 2020

©2020. American Geophysical Union.
All Rights Reserved.

Experimental Insights Into the Interplay Between Buoyancy, Convection, and Dissolution Reaction

A. W. A. Ahoulou¹ , A.-J. Tinet¹ , C. Oltéan¹ , and F. Golfier¹ 

¹Université de Lorraine, CNRS, GeoRessources, Nancy, France

Abstract Predicting the instabilities that occur during the chemical reaction between a percolating fluid and a soluble rock leading to the development of macroscopic channels called wormholes is a key for understanding many geological processes. Their shape and their spatial distribution depend on two dimensionless numbers, namely Damköhler (Da) and Péclet (Pe) numbers. Although the dissolution phenomenon has been extensively studied both in the context of acid stimulation of oil wells in carbonate rocks and carbon capture and storage, few works have focused on the influence of the physical properties of fluids on wormhole patterns. Consequently, through interpretation of images acquired during the injection of pure water into a 2-D reconstituted salt massif and considering different configurations of injection, we illustrate the buoyancy effects on wormhole formation. Contrarily to observation in fractures, experimental results suggest that dissolution regimes can still be described by the classical dimensionless numbers Da and Pe. As for the regime diagram, it remains practically unchanged for strong Péclet and weak Damköhler and undergoes a slowdown of the propagation of the dissolution front when the number of Richardson's increases. Analysis of morphological descriptors such as area, interface, and tortuosity shows that density contrast has an influence on intermediate- to high-Richardson dissolution regimes that may be explained by the existence of buoyancy effects.

1. Introduction

Since the end of the 1990s, marked by experimental works carried out by Daccord (1987) or Hoefner and Fogler (1988), numerous experimental and numerical studies were performed in order to understand the behavior of a dissolution front in porous matrix (Golfier et al., 2002; Soulaïne et al., 2017; Szymczak & Ladd, 2004, 2011). Considered as one fundamental mechanism in geological systems, for example, formation of the karst aquifers (Campana & Fidelibus, 2015; Johnson, 2008; Raines & Dewers, 1997), the chemical dissolution operates also in many geoenvironmental applications such as petroleum engineering (Izgec et al., 2010; Schechter & Gidley, 1969), CO₂ sequestration (Emami-Meybodi et al., 2015), solution mining cavities (Guo et al., 2016; Johnson, 2005; Luo et al., 2012), or hydrogeological systems (Mayer et al., 2002). Indeed, when a fluid phase flows into a porous rock containing soluble minerals (e.g., carbonate or halite grains) not in equilibrium with the solution, it generally dissolves some of the porous matrix creating different types of dissolution patterns. Snippe et al. (2020) suppose that, at large length scale, for a given volume of dissolved calcite obtained by injecting a specified water flow rate and under CO₂-saturated conditions, there are three potential idealized patterns around the injection well: compact, wormholing, and uniform. A fourth possible pattern is derived from the work of Menke et al. (2018) the channeling, defined as “the erosion of preexisting preferential flow paths.” These patterns are similar to those experimentally obtained at the core scale using limestone core samples and HCl injection (Fredd & Fogler, 1998b; Hoefner & Fogler, 1988). Moreover, according to Bazin (2000), Fredd and Fogler (1998a), and Fredd and Miller (2000), these dissolution patterns are the result of a strong interplay between reaction, diffusion, and advection. Using a numerical model developed at Darcy-scale, Golfier et al. (2002) group these mechanisms and these patterns using two dimensionless numbers that are Péclet and Damköhler numbers. The first one is defined as the ratio between the advection and diffusion while the second one generally compares the strength of fluid/solid interface reaction rate to that of molecular diffusion. If Péclet number is very low, involving low advection, the reactive fluid is quickly consumed in the vicinity of the injection surface leading to a compact dissolution pattern. On the other hand, if Péclet number is high enough, the acid solution practically passes through the whole porous medium without being completely consumed leading to the development of a uniform dissolution pattern. Between these two extreme

cases, the variation of Péclet/Damköhler numbers leads to the appearance and the development of high conductive channels known as wormholes. Taking into account their spatial morphology, they can be classified in conical, dominant, and ramified wormholes. Nevertheless, the development of wormholes causes the alteration of the solid matrix and leads to an increase in local permeability and therefore, to an increase in mass transfer. For this reason, in last years, several experimental techniques including injection molding (Fredd & Fogler, 1998b), direct monitoring in 2-D flow cells (Golfier et al., 2002; Oltéan et al., 2013), neutron radiography and X-ray tomography (Gray et al., 2018; Menke et al., 2015) have been developed in order to better characterize the alteration of the rock pore structure. A review of these techniques can be found in the work of Luquot et al. (2016). The main goal of these studies was to establish some correlations between the permeability and porosity, essential parameters in continuum-scale models (Kang et al., 2007). In the same way, the dissolution process is also impacted by mineralogical heterogeneity of rocks (Liang et al., 2015; Liu et al., 2017). It seems that in this case, proposing relationships for hydrological properties is a real challenge (Min et al., 2016).

Reactions between the “injected acidic solutions,” the solid matrix and/or the fluid saturating the porous matrix can also change the physical properties (density, dynamic viscosity, and diffusivity) of the fluids involved. The dissolution of CO₂ in brine is one of the most common examples, and it has received particular scientific attention in the last years (see the recent review of Emami-Meybodi et al. (2015)). In fact, the trapped CO₂ in the upper part of the saline aquifer dissolves in the underlying brine creating a layer denser than the original brine. Under the action of both gravity and density contrast this layer may become gravitationally unstable leading to the apparition and the development of convective cells, labeled the convective regime. Moreover, according to Slim et al. (2013), the temporal evolution of the CO₂ dissolution into an idealized system may be described via six regimes (diffusive, linear-growth, flux-growth, merging, reinitiation, and convective shutdown). The convective mixing can also create an acidic solution that reacts with the solid matrix altering the porosity and the permeability fields of the rock. For a fast chemical dissolution reaction, Hidalgo et al. (2013) show that the dissolution pattern does not exactly follow the propagation of concentration fingers. This phenomenon is particularly localized in the regions characterized by a maximal fluid mixing that corresponds to the flow stagnation points. A similar result, that is, initiation of dissolution in regions of locally high mixing, was obtained by Fu et al. (2015) who studied the dissolution patterns over time resulting from the dissolution of a carbonate rock. Numerical results indicate that these high mixing zones where dissolution occurs also appear far from the concentration front because of the onset of convective cells near the upper boundary.

Taking into account all these comments and discussions, one question remains: What is the impact of the change in the physical properties of the fluids involved on dissolution regimes and more specifically on the regimes mentioned at the beginning of this paragraph? In other words, what is the impact of the buoyancy effects on the dissolution patterns when the carbonate rock is represented by a halite deposit? To our knowledge, works dealing with the effects of density driven on dissolution for a single phase flow are limited. Some studies explored this phenomenon, though considering vertical and/or horizontal fractures (Chaudhuri et al., 2009; Dijk et al., 2002; Luo et al., 2012; Oltéan et al., 2013). They show that, under buoyancy effect, the dissolution patterns depend, in addition to Pe and Da numbers, on the spatial orientation of the fracture relative to the gravity direction, expressed through the Rayleigh, Bond or Richardson numbers. For instance, using a diffusion interface model (DIM) applied to a channel constituted by two parallel salt blocks, Luo et al. (2012) show that the solid-liquid dissolution process strongly depends of Péclet and Rayleigh number. Similarly, using an experimental and numerical study, Oltéan et al. (2013) have constructed a 3-D behavior diagram by highlighting the existence of four dissolution patterns: kinetics, convection, mixed-convection, and buoyancy-dominated dissolution. Other studies, such as Snippe et al.'s (2017), used the buoyancy effects as the main hypothesis to explain some experimental observations from the work of Ott and Oedai (2015). Indeed, in the two-phase CO₂-brine injection experiments carried out by the authors mentioned above, dissolution occurs preferentially in the lower part of the horizontally arranged rock sample. According to Snippe et al. (2017) who used numerical simulations, this configuration can only be assigned to gravity effects.

In this paper, we propose to assess the influence of buoyancy on dissolution patterns via an experimental laboratory study. This study is carried out using a Hele-Shaw cell type in which the space between the plates is filled with a salt granular medium. The dissolution patterns are analyzed by interpreting the images based

on the spatial and temporal evolutions of the dissolved zone obtained by the injection of the pure water. Discussions and conclusions focus on the impact of density contrast on dissolution regimes and the wormhole morphology.

2. Materials and Methods

2.1. Material

The material used in our experiments is constituted by a mixture of 90% salt grains (NaCl) and 10% of gypsum plaster ($\text{CaSO}_4, \frac{1}{2} \text{H}_2\text{O}$) to enforce its cohesion. Both materials are crushed and screened to a particle size of 80 to 125 $\mu\text{m} \pm 1\%$ before mixing. Direct shear test is carried out to determine the shear strength parameters of this two-component material, that is, the cohesive strength c (Pa) and the internal angle of friction φ ($^\circ$). Under fully drained conditions, values of $c = 42$ kPa and $\varphi = 32^\circ$ were measured. Within the range of injection flow rates of interest, a straightforward estimate of the maximal shear stress value reached in the wormhole suggests that mechanical effects can be discarded. Even if evidences of erosion by rolling and sliding of grains at the wormhole walls have been observed at the highest injection velocities, these ones are assumed to be negligible relative to dissolution mechanisms.

Salt and gypsum have similar reaction rate constants (2.4×10^{-6} m/s for salt and 4.5 to 9×10^{-6} m/s for gypsum) (Colombani, 2008; Dutka et al., 2020; Weisbrod et al., 2012) even if addition of surfactant in commercial plaster may significantly reduce the reaction rate value. However, the solubility of salt and plaster is significantly different (358.5 g/L for salt and 2.5 g/L for gypsum) and may lead to a differentiated dissolution for both materials at low velocity.

2.2. Experimental Setup and Protocol

The experimental device is presented in Figure 1. It consists in a set of parallel transparent glass plates of size (10 cm \times 22 cm) and thickness 1 cm, encased in an aluminum frame. This system ensures the rigidity of the cell as well as allows both horizontal and vertical placement of the device. The two glass plates are separated by a distance of $e = 0.05$ cm with separators of width 2 cm and laterally sealed with silicone. Therefore, the useful volume of the cell is of 27 cm³. Top and bottom tanks are added to allow in and outflow in the apparatus. The tanks are filled with glass beads and a geotextile is added to ensure homogeneous fluid injection across the width of the cell.

The test protocol consists in the following:

- Filling of the cell with dry material up to a porosity of around 43%, leading to a permeability of around 5×10^{-12} to 1.5×10^{-11} m², as estimated using both Hazen empirical formula and Kozeny–Carman equation. The wormhole permeability is limited by the spacing between plates and it is about 2.1×10^{-8} m² as obtained from the cubic law ($e^2/12$). We note that, in order to assure a certain reproducibility of the cell filling, the salt grains were packed uniformly from the upper part of the cell and the porous medium thus obtained was compacted using a vibrating table.
- Saturation with water oversaturated with salt (at solubility 358.5 g/L) is performed vertically, from bottom to top, through application of a gradually increasing water head.
- Injection of undersaturated water with a given salt concentration and at a given constant flow rate using a syringe pump. In vertical configuration, injection is performed from bottom to top to ensure density-driven contrast.

The dissolution front was monitored using a digital camera allowing an image size of 4,614 \times 3,744 pixels and with backlighting so as to improve the image quality (Figure 1). The rate of data acquisition (i.e., number of images/minute) is adapted to the flow rate imposed. It varies between 40 and 1,200 images for each test. A calibration of the images is carried out for each test leading to an average resolution value of 1 pixel/68 μm .

2.3. Image Treatment

Image acquired during dissolution tests are processed in order to allow for morphological qualitative and quantitative comparison. This processing was performed using the software ImageJ and aims at transforming the raw data into segmented images with two phases (dissolved and nondissolved), eventually three (dissolved, partially dissolved, and nondissolved). To this end, the raw data for a given test is cropped in order to remove nonrelevant sections such as reservoirs or lateral edges of the cell. The images are then filtered

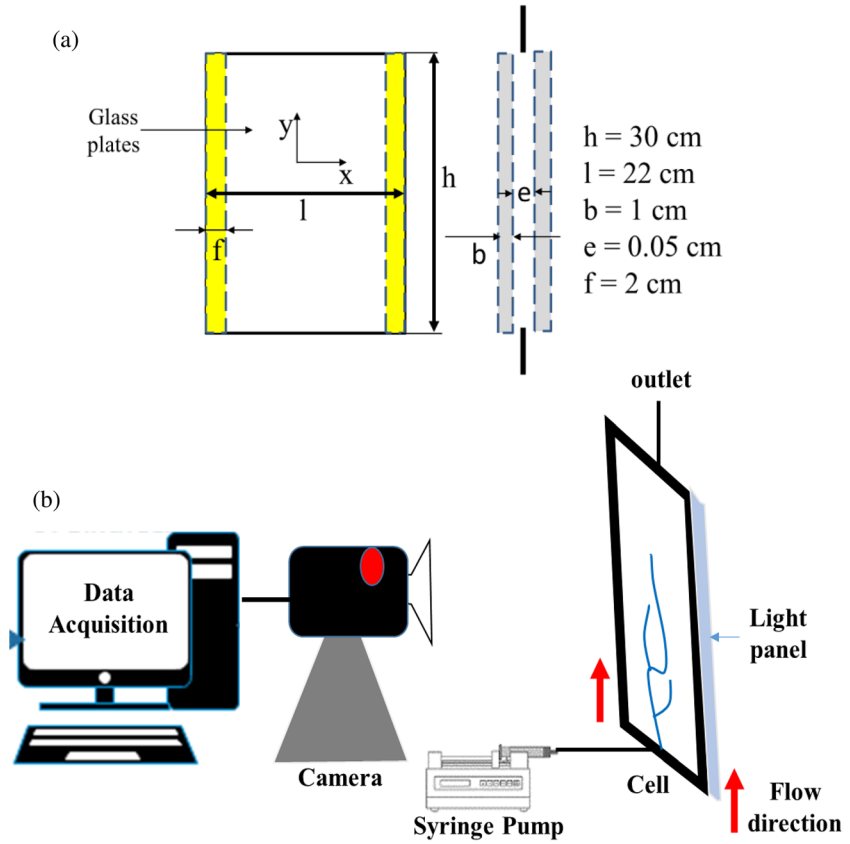


Figure 1. (a) Hele-Shaw type cell; (b) experimental setup illustrated in vertical configuration.

using a median filter with 10 pixels radius so as to limit noise appearing during acquisition. After transformation of the colored images to gray scale, the image prior to injection is subtracted. Such an operation allows removing artifacts that are generated either by the filling process, such as layering, or by image acquisition, such as a vertical gradient of the gray levels, as seen in Figure 2. Finally, images are segmented using a threshold-based method. When only two phases (dissolved and nondissolved) are considered, the threshold value is the same for all tests. For the sake of clarity and illustrations, recolored images will be used hereafter for contrast enhancement and to help visualize porosity gradients.

2.4. Dimensionless Quantities

As described in section 1, dimensionless numbers are often used to compare the influence of different phenomena. In the following, the local Péclet, Dämmkohler, and Richardson numbers, defined in (Equation 1) will be used.

$$Pe = \frac{UL}{D}; \quad Da = \frac{\alpha L}{U}; \quad Ri = \frac{L \Delta\rho g}{\rho_0 U^2} = \left(\frac{U_b}{U}\right)^2 \quad (1)$$

with L (m) the characteristic length represented by the square root of the initial permeability, U (m s^{-1}) the pore velocity, D ($\text{m}^2 \text{s}^{-1}$) the molecular diffusion, α the effective dissolution rate or mass transfer coefficient (s^{-1}), g (m s^{-2}) the gravitational acceleration, $\Delta\rho = \rho - \rho_0$ (kg m^{-3}) the maximum density variation and ρ_0 (kg m^{-3}) the reference fluid density (pure water in the present case). As shown in (Equation 1), the Richardson number compares the buoyancy velocity U_b to the pore velocity. The latter is computed by dividing the injection rate by the pore cross-sectional area (in the present case 18 cm^2 multiplied by the porosity). It should be noted that the dimensionless quantities were computed considering the medium initial conditions and therefore do not take into consideration the properties evolution as the dissolution advances.

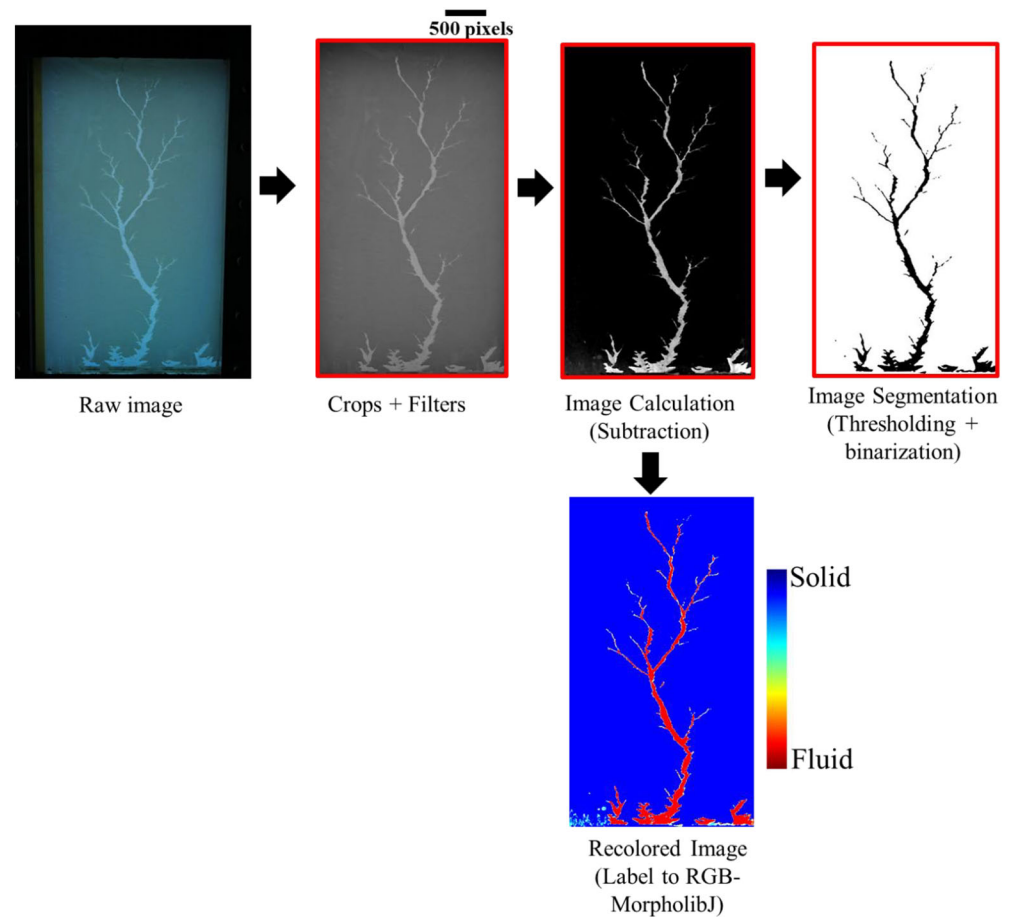


Figure 2. Image treatment (processing and binarization) (top row). On the bottom row is an illustration of recoloring of grayscale image used to visually enhance contrasting.

2.5. Morphological Descriptors

To analyze the dissolution patterns several morphological descriptors are used (dissolved area and perimeter, front velocity, as well as tortuosity). Their calculation is performed using ImageJ and ImageJ plugin MorphoLibJ (Lehmann & Legland, 2012). Thus, the dissolved area is computed straightforwardly as the amount of pixels in the dissolved phase. The interface between dissolved and nondissolved phases, or perimeter, is computed using the Cauchy-Crofton algorithm (Lehmann & Legland, 2012). The front of the dissolved area corresponds to the position of the dissolved phase pixel located the farthest from the injection face. It is tracked on a set of 10 to 20 images between the beginning of dissolution and the breakthrough. In order to perform tortuosity and ramification angles calculations, the dominant wormhole, when existing, is selected on the image at breakthrough. The tortuosity corresponds to the ratio of shortest length between the injection and the outlet faces through the dissolved phase to the length of the image. The former is computed by generating the skeleton of the dominant wormhole and by measuring the shortest length of the skeleton segments required to join the injection and outlet faces.

3. Results and Discussions

Dissolution is studied in both horizontal and vertical configurations under several different injected flow rates ranging from 0.1 to 500 ml/hr (0.1, 1, 2, 5, 10, 13, 40, 100, and 500 ml/hr). We have considered an injected solution of pure water so as to maximize the effect of density contrast. In order to assess the replicability of the results, each experiment is repeated (an extra repetition is performed for 1 ml/hr). However, considering that the dissolution is triggered by local heterogeneity of the porous medium and that the

Table 1
Experimental Case Studies Properties

Name	Q_{inj} (ml hr ⁻¹)	ϵ (-)	K ($\times 10^{-11}$ m ²)	Pe	Da	Ri
Horizontal configuration						
BH0.1	0.1	0.40	0.99	0.0024	41	—
BH1	1	0.44 ± 0.02	1.60 ± 0.29	0.03 ± 0.0012	5.74 ± 0.71	—
BH2	2	0.42 ± 0.0	1.2 ± 0.0	0.0514 ± 0.0	2.38 ± 0.0	—
BH5	5	0.44 ± 0.04	1.53 ± 0.62	0.135 ± 0.015	1.11 ± 0.3	—
BH10	10	0.435 ± 0.015	1.35 ± 0.25	0.27 ± 0.01	0.54 ± 0.06	—
BH13	13	0.40 ± 0.0	0.99 ± 0.0	0.32 ± 0.0	0.31 ± 0.0	—
BH40	40	0.375 ± 0.015	0.76 ± 0.13	0.90 ± 0.04	0.0835 ± 0.0105	—
BH100	100	0.43 ± 0.01	1.35 ± 0.15	2.65 ± 0.05	0.0515 ± 0.0035	—
BH500	500	0.46	1.9	14	0.013	—
Vertical configuration						
BV0.1	0.1	0.42 ± 0.03	1.345 ± 0.355	0.0026 ± 0.0002	49 ± 11	1.3 ± 0.4 × 10 ⁷
BV1	1	0.43 ± 0.03	1.45 ± 0.45	0.0275 ± 0.0035	5.26 ± 1.16	1.45 ± 0.45 × 10 ⁵
BV2	2	0.41 ± 0	1.1 ± 0	0.0499 ± 0	2.2029 ± 0	2.87 ± 0 × 10 ⁴
BV5	5	0.44 ± 0.03	1.6 ± 0.5	0.135 ± 0.015	1.63 ± 0.25	6.55 ± 1.75 × 10 ³
BV10	10	0.435 ± 0.015	1.45 ± 0.25	0.27 ± 0.01	0.54 ± 0.06	1.5 ± 0.2 × 10 ³
BV13	13	0.405 ± 0.035	1.1 ± 0.4	0.32 ± 0.03	0.34 ± 0.09	6.8 ± 2.4 × 10 ²
BV40	40	0.40 ± 0.01	0.995 ± 0.105	0.97 ± 0.03	0.102 ± 0.008	65.02 ± 6.75
BV100	100	0.43 ± 0.01	1.35 ± 0.15	2.65 ± 0.05	0.0515 ± 0.0035	14 ± 1
BV500	500	0.41	1.1	12	0.0088	0.46

phenomena studied are instable, there is a natural variability of the results due to the porous medium construction. As a consequence, two sets of experiments cannot be directly superimposed. Reproducibility will therefore be particularly taken into account with regard to the dissolution patterns, and the significance of a parameter comparison between different test configurations will be made with consideration of the variability between the minimum and maximum values of said parameter for a given test condition.

A summary of the experiments is provided in Table 1. As specified in section 2.4, the Péclet, Damköhler, and Richardson numbers are calculated locally, considering the pore velocity based on the injected flow rate Q_{inj} , cross section (0.9 cm²), and porosity ϵ , the characteristic length is the square root of the permeability K , the molecular diffusion of 10^{-9} m s⁻², the relative variation of density ($\Delta\rho/\rho_0 = 0.2$) corresponding to the variation between pure water and oversaturated brine and the gravity acceleration of 9.8 m² s⁻¹. Measurement of the effective dissolution rate remains quite complex due to the competition between reaction kinetics and mass transfer limitations (Dutka et al., 2020), especially considering the mixed nature of our medium. Since the Péclet numbers are relatively low, the dissolution rate is considered constant and taken equal to 10 s⁻¹ using correlations provided in Appendix B of Golfier et al. (2002). The permeability is computed using Kozeny–Carman equation (K [m²] = $\frac{\epsilon^3 D_{50}^2}{180(1 - \epsilon)^2}$; Bear, 1972) with D_{50} chosen as 100 μ m.

The set of morphological parameters used to describe the dissolution patterns are summarized in Table 2.

The dissolved area and perimeter are provided at breakthrough when available during the experiment duration. The front velocity (or tip velocity) and the “compactness” (ratio of dissolved area to parameter) are obtained through a linear regression along the experiment duration, with the regression coefficient R^2 being provided in Table 2. Overall, all regression coefficients remain high leading to good confidence in the choice of linear approximation and therefore in the obtained velocity and compactness values.

The evolution of the volume of injected water to reach breakthrough normalized by the cell pore volume (or PVBT) versus injected flow rate (Figure 3) is an essential step in the interpretation of acid injection in laboratory and/or numerical experiments (Chen et al., 2018; Cohen et al., 2008; Golfier et al., 2002; Panga et al., 2005).

Table 2
Morphological Properties

Name	Front velocity (cm s ⁻¹)	R ² (velocity)	Dissolved area <i>S</i> (BT) (cm ²)	Dissolved perimeter <i>P</i> (BT) (cm)	Average <i>S/P</i> (cm)	R ² (<i>S/P</i>)
Horizontal configuration						
BH0.1	1.0 × 10 ⁻⁵	0.967	-	-	0.29	0.910
BH1	2.0 ± 1 × 10 ⁻⁴	0.950 ± 0.036	-	-	0.44 ± 0.05	0.956 ± 0.033
BH2	4.5 ± 0.5 × 10 ⁻⁴	0.985 ± 0.006	-	-	0.41 ± 0.12	0.808 ± 0.078
BH5	2.65 ± 0.33 × 10 ⁻³	0.985 ± 0.014	25.23 ± 6.07	289.74 ± 14.7	0.088 ± 0.018	0.991 ± 0.004
BH10	7.6 ± 0.3 × 10 ⁻³	0.995 ± 0.003	31.4 ± 0.5	384 ± 85	0.08 ± 0.02	0.9965 ± 0.0005
BH13	6.55 ± 0.45 × 10 ⁻³	0.935 ± 0.042	22.3 ± 1.66	328 ± 26	0.065 ± 0.015	0.996 ± 0.002
BH40	2.35 ± 0.05 × 10 ⁻²	0.9941 ± 0.0001	21.61 ± 0.41	281.5 ± 58.5	0.08 ± 0.02	0.998 ± 0
BH100	5.65 ± 0.45 × 10 ⁻²	0.964 ± 0.022	29.7 ± 3.8	195 ± 15	0.17 ± 0.01	0.9875 ± 0.0065
BH500	2.4 × 10 ⁻¹	0.928	34.7	114	0.31	0.945
Vertical configuration						
BV0.1	9.5 ± 0.5 × 10 ⁻⁶	0.989 ± 0.004	-	-	0.19 ± 0.05	0.9625 ± 0.0315
BV1	1.35 ± 0.65 × 10 ⁻⁴	0.974 ± 0.044	-	-	0.16 ± 0.12	0.987 ± 0.007
BV2	3.0 ± 0 × 10 ⁻⁴	0.973 ± 0.005	-	-	0.095 ± 0.005	0.9535 ± 0.0205
BV5	2.4 ± 0 × 10 ⁻³	0.994 ± 0.001	20.84 ± 0.46	330.5 ± 12.5	0.06 ± 0	0.9865 ± 0.0085
BV10	9.6 ± 0.14 × 10 ⁻³	0.995 ± 0.004	21.55 ± 2.85	220 ± 19	0.095 ± 0.005	0.993 ± 0.005
BV13	9.55 ± 0.45 × 10 ⁻³	0.987 ± 0.002	21.49 ± 0.66	253.36 ± 13.83	0.07 ± 0	0.9455 ± 0.0285
BV40	2.75 ± 0.15 × 10 ⁻²	0.9905 ± 0.0045	19.245 ± 3.615	257.24 ± 28.65	0.06 ± 0.01	0.903 ± 0.089
BV100	6.05 ± 0.35 × 10 ⁻²	0.9795 ± 0.0045	27.65 ± 0.05	163 ± 4	0.185 ± 0.015	0.960 ± 0.036
BV500	2.3 × 10 ⁻¹	0.723	33.6	170	0.17	0.875

Note. R² is the regression coefficient. Lack of value means that the breakthrough (BT) was not reached during the duration of the experiment.

As shown in Figure 3, the PVBT for both configurations demonstrates classic behavior with the same optimal value, that is, around 10 ml/hr. However, it should be noted that, to the left of the minimum, the PVBT for the vertical configuration is located above the PVBT for the horizontal configuration (Figure 3), while to its right this trend is seemingly reversed and attenuated. In other words, the density contrast effects are mostly significant for the PVBT at low injection rates, that is, high Richardson numbers. This behavior seems to be contradictory to our a priori expectations. Indeed, given the high values of Richardson number (Table 2) and assuming a 1-D behavior, we would have thought that the buoyancy effect, that acts as an upward force as the forced convection, would “accelerate” the dissolution in the vertical direction resulting in a downward shift of the vertical configuration PVBT curve prior to the minimum. In order to better understand this unexpected result, we will investigate further the influence of cell orientation, and therefore buoyancy, on the dissolution patterns and dynamics and discuss the cause of the shift of PVBT using morphological descriptors as well as direct observations. This discussion will be organized according to the three different sections on the PVBT curve. At low Richardson ($Ri < 100$, i.e., $Q_{inj} \geq 40$ ml/hr in the present experiment) where the PVBT increases with injected flow rate (Figure 3), at intermediate Richardson ($10^2 < Ri < 10^4$, i.e., Q_{inj} around 10 ml/hr) when the PVBT is close to optimum and finally, at high Richardson ($Ri > 5 \cdot 10^4$, i.e., $Q_{inj} \leq 2$ ml/hr) where the PVBT under horizontal configuration is above the PVBT under vertical configuration.

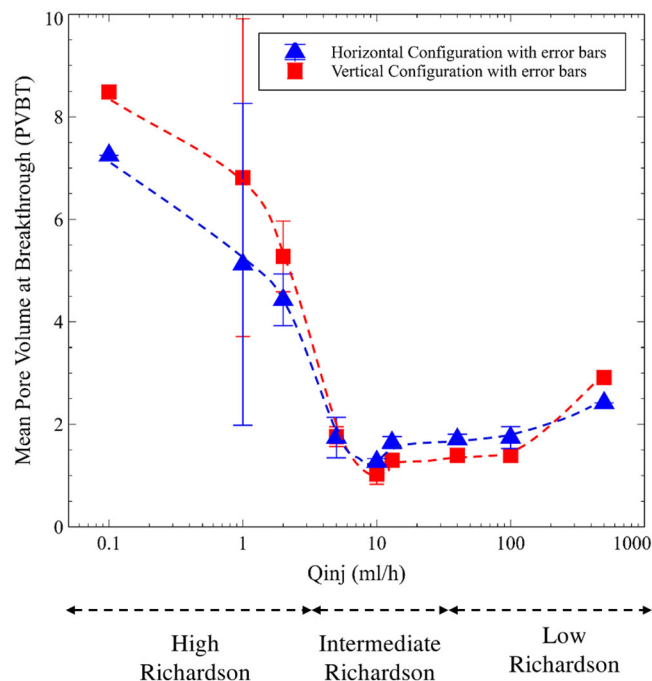


Figure 3. Mean pore volume at breakthrough (PVBT) curve for both configurations.

3.1. Low Richardson

In Figures 4, 5, and 6 are presented the dissolution patterns at breakthrough for a given experiment at flow rates of 500, 100, and 40 ml/hr,

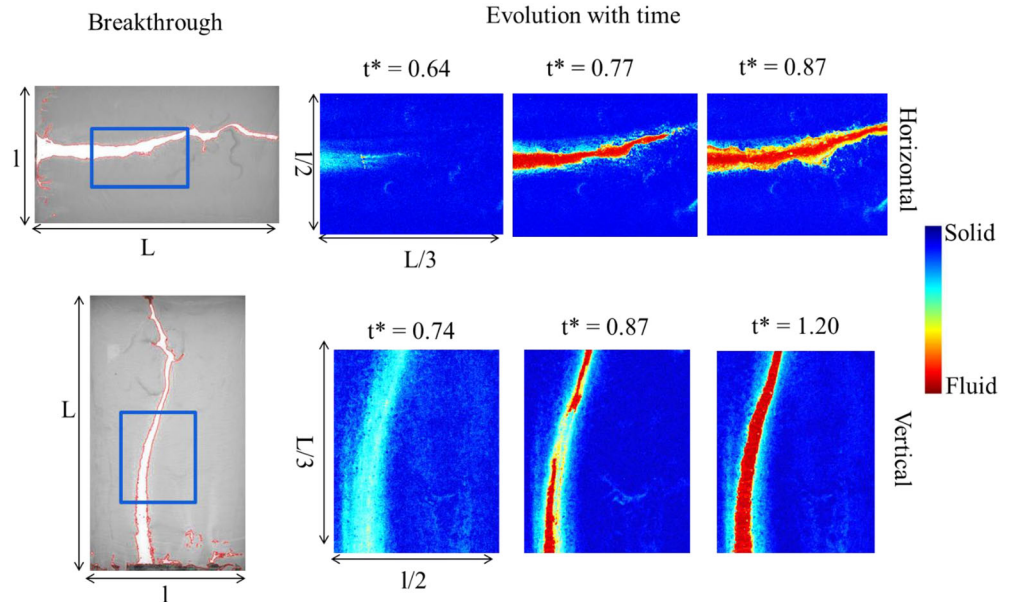


Figure 4. Dissolution pattern for the flow rate 500 ml/hr in horizontal (BH500) (top) and vertical (BV500) (bottom) ($Ri = 4.6 \times 10^{-1}$) configurations. (left) Grayscale image at breakthrough, the red line represents the interface between dissolved area and nondissolved area as obtained from the segmentation. Blue rectangle locates the zoomed area. (right) Recolored zoomed images of dissolution at different times relative to the initial image.

respectively (Richardson below 100 for the latter and below unity for 500 ml/hr flow rate), for both horizontal and vertical configurations. On the right side of these figures, a zoomed view of the dissolution process along dimensionless time t^* (volume of injected water at a given time normalized by the cell volume) is shown.

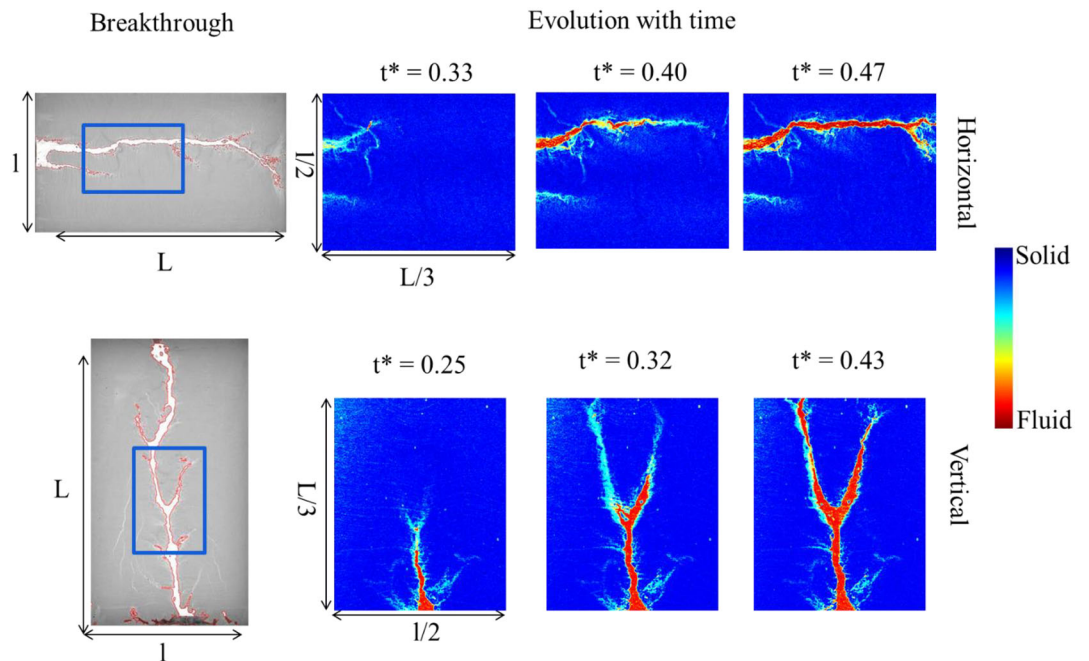


Figure 5. Dissolution pattern for the flow rate 100 ml/hr in horizontal (BH100) (top) and vertical (BV100) (bottom) ($Ri = 1.3 \times 10^1$) configurations. (left) Grayscale image at breakthrough, the red line represents the interface between dissolved area and nondissolved area as obtained from the segmentation. Blue rectangle locates the zoomed area. (right) Recolored zoomed images of dissolution at different times relative to the initial image.

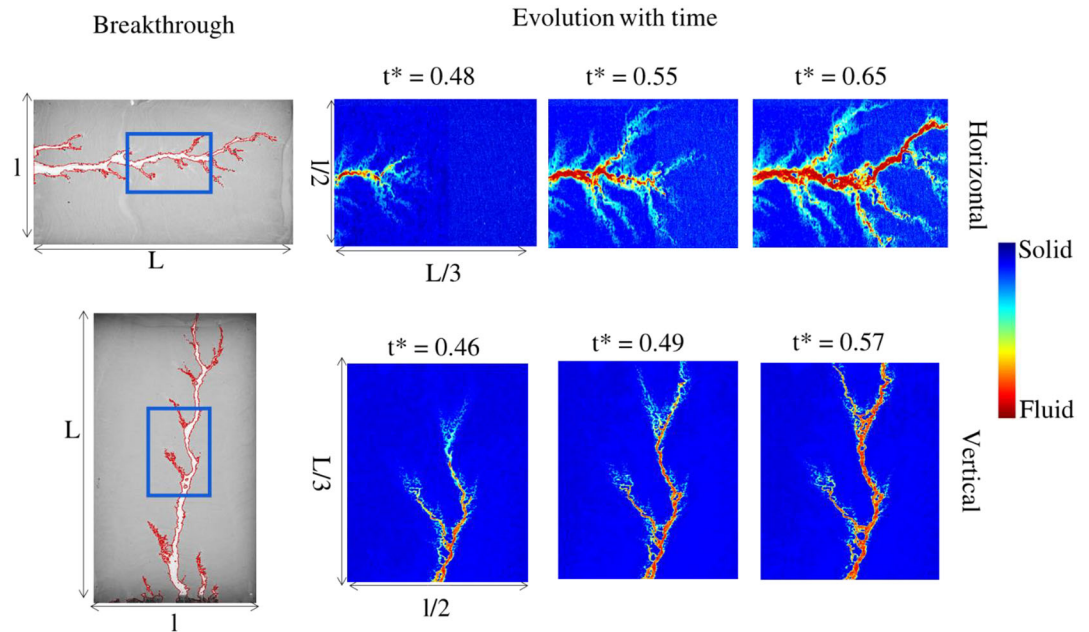


Figure 6. Dissolution pattern for the flow rate 40 ml/hr in horizontal (BH40) (top) and vertical (BV40) (bottom) ($Ri = 7.1 \times 10^4$) configurations. (left) Grayscale image at breakthrough, the red line represents the interface between dissolved area and nondissolved area as obtained from the segmentation. Blue rectangle locates the zoomed area. (right) Recolored zoomed images of dissolution at different times relative to the initial image.

For all these flow rates, a principal wormhole develops in the medium presenting at its end a transition zone between the dissolved and nondissolved area (blue sky area, Figures 4 to 6) indicating the existence of a porosity gradient. At 40 and 100 ml/hr flow rate (Figures 4 and 5), this principal wormhole presents some secondary branches of short lengths exhibiting the same property than the principal wormhole, that is, transition zone between the dissolved and nondissolved area. Due to these specificities (presence of secondary branches and porosity gradient) and by analogy with Fredd and Fogler (1998b), Fredd and Miller (2000), and Golfier et al. (2002), we can consider that the pattern is transitioning toward the ramified regime. However, given the relatively small extent of the transition zone, the pattern may still be related to the dominant regime and, therefore, it will be hereafter called “dominant/transition.” The analysis of quantitative data shows that the experimental results for all configurations remain very similar. Indeed, as the PVBT curves in horizontal and vertical configurations tend to converge toward one another, the front velocities are also rather similar with generally a mean velocity slightly higher for the vertical configuration compared to the horizontal configuration (maximum 15%). This observation is not valid for the highest flow rate where the two front velocities are rather identical. Concerning the mean dissolved areas at breakthrough, we can consider that the results show good reproducibility. Indeed, with one exception concerning the vertical configuration for $Q_{inj} = 40$ ml/hr, the variability in these surface values between the replicas is less than 10%. For the 100 ml/hr flow rate, the similarity between the vertical configuration and the horizontal configuration is also maintained for the perimeters at breakthrough and for the average surface area-perimeter ratio. On the other hand, for the flow rate of 40 ml/hr, the variability of this descriptor between replicates can reach differences close to 50% although the dissolved areas are relatively identical (e.g., horizontal configuration). This difference is certainly due to the length and width of the wormholes that, in the one experiment, are longer and less wide than in the other experiment (not represented in this paper). It means that the slightest variation of the permeability/porosity of the porous medium leads to change of the wormhole morphology. A similar observation was derived for the flow rate of 500 ml/hr. Although the dissolved areas are practically the same, the perimeter of the dissolved phase in the vertical configuration is significantly higher than the one for the horizontal configuration. Actually, observation of the raw image (Figure 4) shows that, at the bottom of the cell, the dissolution is spread wider under vertical configuration, with smaller wormholes. This observation is also noted for two other flow rates, but less

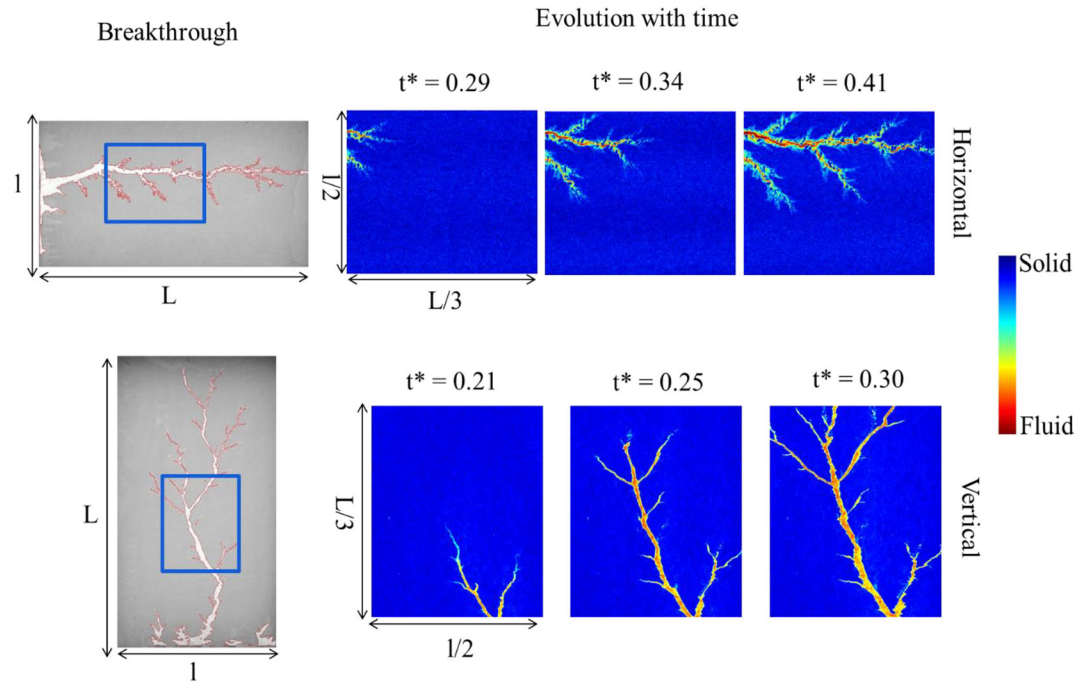


Figure 7. Dissolution pattern for the flow rate 10 ml/hr in horizontal (BH10) (top) and vertical (BV10) (bottom) ($Ri = 1.3 \times 10^3$) configurations. (left) Grayscale image at breakthrough, the red line represents the interface between dissolved area and nondissolved area as obtained from the segmentation. Blue rectangle locates the zoomed area. (right) Recolored zoomed images of dissolution at different times relative to the initial image.

significantly. Such an observation suggests that at the beginning of the dissolution, there is more competition between different wormholes in the vertical configuration than in the horizontal configuration. Therefore, at the injection face, buoyancy may have an impact on the amount of wormholes initiated; however, as soon as the main wormhole develops the differences between the horizontal and vertical configuration become negligible. In other words, the influence of density contrast is quickly canceled out by forced convection, as illustrated by the low Richardson's number, as soon as preferential flow paths develop.

3.2. Intermediate Richardson

Between 5 and 20 ml/hr, the optimal value of the PVBT curve is reached for both horizontal and vertical configuration around 10 ml/hr (Figure 3). The dissolution pattern is clearly a “dominant regime,” following the classification of Fredd and Miller (2000), Golfier et al. (2002), and Hoefner and Fogler (1988). We will call it “dominant/optimal regime.” In our case, this regime is characterized by the development of a mean wormhole from which starts the formation of many branches of different lengths (Figure 7). In the vertical configuration the interface between dissolved and nondissolved zone is relatively sharp while in the horizontal configuration a transition zone is yet observed, represented by a partially dissolved zone enveloping the branches, highlighting the existence of a porosity gradient. On top of that, in the vertical configuration, the dominant wormhole presents a larger tortuosity (about 1.10 for vertical configuration and compared to 1.04 for horizontal configuration) and a lower thickness (average diameter along the wormhole of 0.42 to 0.64 cm for BV10 compared to 0.82 to 0.91 cm for BH10). Moreover, the branches are more developed, longer, and more numerous in the vertical case (Figure 7).

If our attention is focused on the configurations obtained for $Q_{inj} = 5$ ml/hr, the observations and comments mentioned above cannot be made similarly (Figure 8). First, the tortuosity values for the dominant finger in both configurations are practically the same (1.01 to 1.05). Second, the partially dissolved zone around the branches and therefore the porosity gradient exists for both configurations. Moreover, if we analyze the area close to the injection surface, we observe for the vertical configuration the apparition of small “wormholes” characterized by a strongly irregular interface between dissolved and nondissolved areas. As this peculiarity was not captured for the horizontal configuration, it is certainly due to the density contrast.

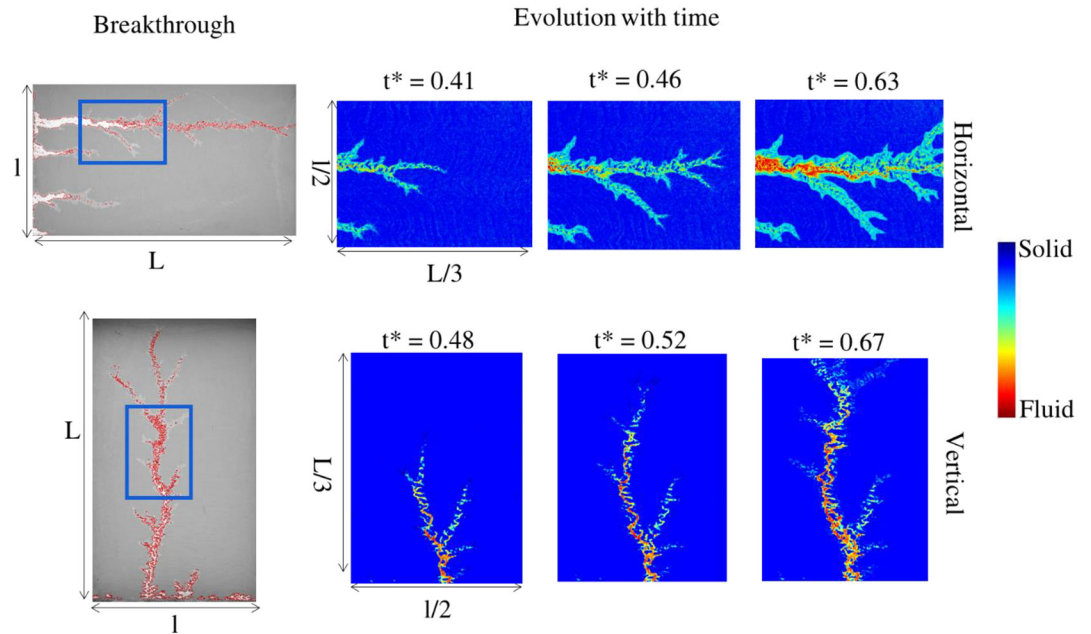


Figure 8. Dissolution pattern for the flow rate 5 ml/hr in horizontal (BH5) (top) and vertical (BV5) (bottom) ($Ri = 8.3 \times 10^3$) configurations. (left) Grayscale image at breakthrough, the red line represents the interface between dissolved area and nondissolved area as obtained from the segmentation. Blue rectangle locates the zoomed area. (right) Recolored zoomed images of dissolution at different times relative to the initial image.

Concerning the front velocity, for $Q_{inj} \geq 10$ ml/hr it keeps the same characteristic as that observed for low Richardson numbers, that is, it is higher in the vertical configuration. For some experiments, the difference between vertical and horizontal configurations can be relatively high (e.g., 46%) even if the porosities are the same (e.g., BH10 and BV10). On the other hand, for $Q_{inj} = 5$ ml/hr, the mean velocity ratio is inverted (mean velocity vertical configuration/horizontal configuration ≈ 0.85). By taking into account these two particularities, that is, (i) the apparition of the irregular interface between dissolved and nondissolved areas and (ii) the reversal of the mean velocity ratio, it seems to us quite relevant to consider that the transition zone corresponding to the influence of the density contrast is located between $Q_{inj} = 5$ ml/hr and $Q_{inj} = 10$ ml/hr, that is, $10^3 < Ri < 10^4$.

In regard to the other morphological parameters and taking into account the observations on velocity, we first analyze the experiments with $Q_{inj} = 10$ ml/hr and $Q_{inj} = 13$ ml/hr. Both the surface and perimeter at breakthrough presents the same variation with that mentioned for low Richardson numbers, that is, smaller for vertical configurations (e.g., for BV10 compared to BH10 by 24% and 20%, respectively). However, the ratio of surface to perimeter remains practically identical between vertical and horizontal configuration. Moreover, one of the BV10 experiments, that has a higher porosity, demonstrates lower velocity, surface, and perimeter at breakthrough compared to another BV10 experiment. The lower velocity may be related to the higher porosity as, since the flow rate is identical, the pore velocity induced by this flow rate is inversely related to the porosity. Considering that the porosity of BH10 and BV10 are very similar, this previous explanation cannot be used to support the significant difference in front velocity between the two configurations. These differences may be related to structural changes in the porous medium after saturation. Similarly, it should be noted that, for these configurations, the repeatability of the experiments in term of perimeter at breakthrough is difficult to insure. Indeed, if the values of the surfaces show differences of less than 20%, for perimeters the differences can reach 50%.

For $Q_{inj} = 5$ ml/hr, if the dissolved surfaces at breakthrough are practically identical for both configurations (less than 3%) the perimeters are smaller for horizontal configuration (Table 2). In others words, in the same manner as the dissolution front velocity, we observe some shift in trend. Moreover, this result is in agreement with our comments related to the experimental observations concerning the appearance, for vertical configuration and in the area close to the injection section, of small “wormholes” characterized by a

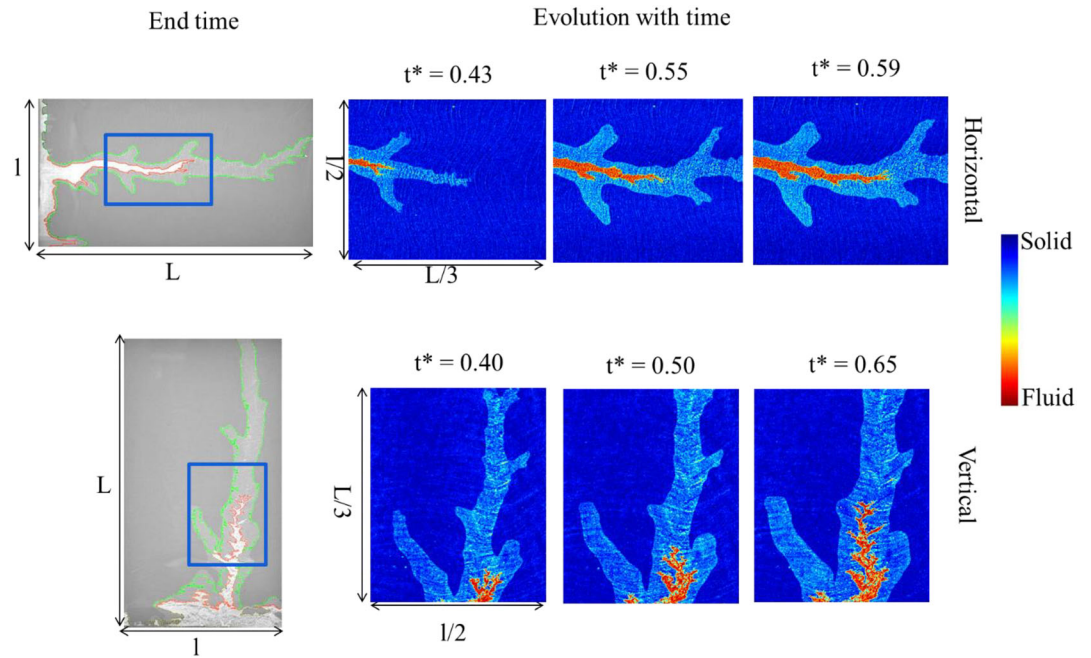


Figure 9. Dissolution pattern for the flow rate 1 ml/hr in horizontal (BH1) (top) and vertical (BV1) (bottom) ($Ri = 1.0 \times 10^5$) configurations. (left) Grayscale image at the final time of the experiment, the red (green) line represents the interface between dissolved area and partially-dissolved area (partially dissolved and nondissolved areas) as obtained from the segmentation. Blue rectangle locates the zoomed area. (right) Recolored zoomed images of dissolution at different time relative to the initial image.

strongly irregular interface between dissolved and nondissolved areas. As already mentioned, this roughness can only be due to the appearance and development of hydrodynamic instabilities generated by the density contrast. In our opinion, the interval between $Q_{inj} = 5$ and $Q_{inj} = 10$ ml/hr, corresponds to a transition zone marked by the influence of hydrodynamic instabilities on the instabilities generated by dissolution. This hypothesis is also supported by the PVBT analysis (Figure 3) which suggests, via the intersection of the curves at $Q_{inj} = 5$ ml/hr, that the range from which density contrast plays an essential role on the dissolution regimes is around $Q_{inj} = 5$ ml/hr. We will investigate in more detail the onset of the instabilities and of the solutal convection induced by dissolution in the following section.

3.3. High Richardson

At a flow rate of 1 and 2 ml/hr the dissolution pattern corresponds to the “conical regime.” It is characterized by a wide base close to the injection cross section, larger for 1 ml/hr than 2 ml/hr (Figure 9).

As shown in Figure 9, at 1 ml/hr, two distinct dissolution zones may be observed. Unlike in the “dominant/transition regime” where the transition from the wormhole to the porous media is rather smooth, the interfaces between the different zones are sharp. The inner wormhole is completely transparent, similarly to the wormholes observed under the other regimes, and thus corresponds to a total dissolution of the porous medium. The second one, which completely surrounds the inner wormhole, corresponds to a partially dissolved zone. Similar behavior has already been mentioned during the analysis of the dissolution pattern at intermediate Richardson ($Q_{inj} = 10$ ml/hr—horizontal configuration and $Q_{inj} = 5$ ml/hr for both configurations). This halo is also observed, albeit much less developed and mostly under horizontal conditions, at flow rate 0.1 ml/hr (Figure 10). It should be noted that, as the injection rate decreases, this envelope thickens laterally with respect to the inner vortex for the vertical configuration, while for the horizontal configuration it develops mostly at the end of the inner vortex (e.g., $Q_{inj} = 1$ ml/hr, Figure 9). As a consequence, the surface of the halo becomes larger under vertical configuration (57 to 63 cm²) compared to horizontal one (40 to 52 cm²) at the envelope breakthrough. The time-averaged envelope tip velocity as well as ratio between surface and perimeter are very close under horizontal and vertical configurations (between 4 and 5 μ m/s for tip

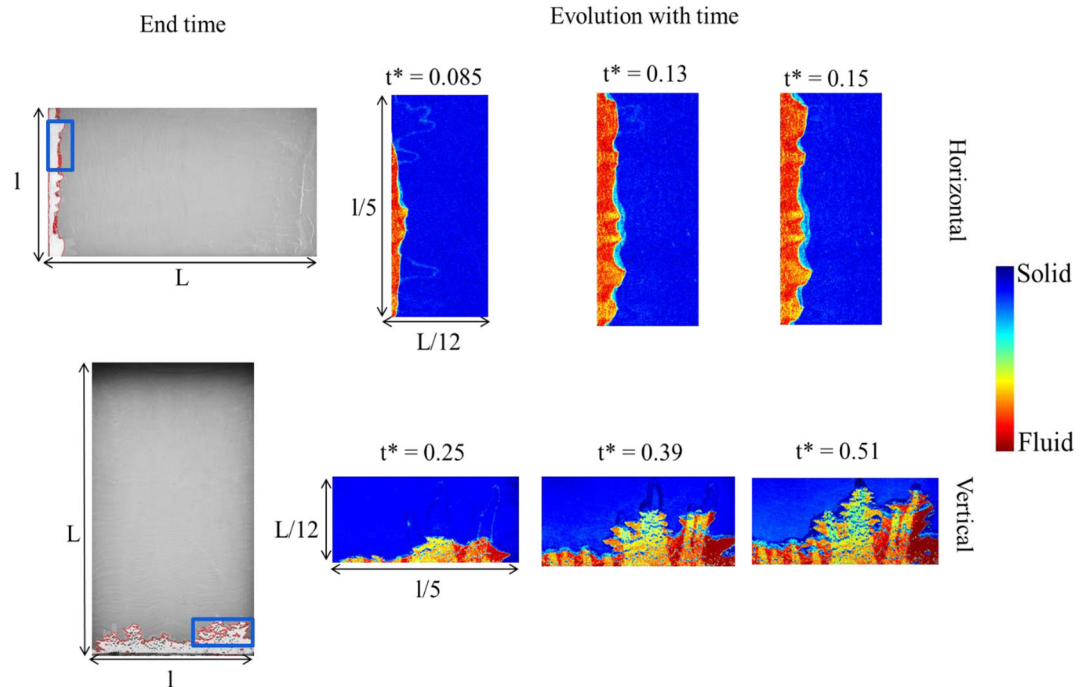


Figure 10. Dissolution pattern for the flow rate 0.1 ml/hr in horizontal (BH0.1) (top) and vertical (BV0.1_2) (bottom) ($Ri = 1.7 \times 10^7$) configurations. (left) Grayscale image at final time of the experiment, the red line represents the interface between dissolved area and non-dissolved area as obtained from the segmentation. Blue rectangle locates the zoomed area. (right) Recolored zoomed images of dissolution at different time relative to the initial image.

velocity and 0.04 cm for compacity) demonstrating an overall similar shape of this partially dissolved area. However, it should be mentioned that some variability in the envelope tip velocity data was observed. Thus, for the vertical configuration, the differences in the envelope tip velocity between the three experiments carried out with $Q_{inj} = 1$ ml/hr, can reach even 100%. For the horizontal configuration, the difference is about 25%. Since the porous medium between the horizontal and vertical configurations have practically the same porosity and permeability characteristics (Table 2), it is possible that these differences are induced by the density contrast via the unstable development of the completely dissolved zone.

As the apparition and the development of this envelope occurs under both configuration and it was not observed in experiments using pure salt (Golfier et al., 2002) or pure plaster (Daccord, 1987), the main hypothesis to explain such observation is that it is linked with the mixed nature of the porous media (salt and plaster) and the subsequent differences in solubility.

Considering now the inner wormhole, we observe that, for the considered flow rates (0.1, 1, and 2 ml/h), the fluid–solid interface demonstrates clear discrepancy between the horizontal and vertical configuration (Figures 9 and 10). Indeed, in the former, the interface remains smooth while in the latter, it has more roughness. This observation is further supported by comparing the surface to perimeter ratio. If attention is paid to the dynamics of the dissolved surface we observe that, for a given surface, the perimeter is about 2.0 times larger (or more for the $Q_{inj} = 2$ ml/hr) in vertical configuration. In the conical regime, the time-averaged front velocity is seemingly lower in vertical configuration in average. However, similarly to the envelope, there is a strong variability with tip velocity ranges mostly overlapping between horizontal and vertical configurations at $Q_{inj} = 1$ ml/hr. Variability is much smaller for $Q_{inj} = 2$ ml/hr, yet the differences in velocity front can reach 50%. This trend is in agreement with that already observed for $Q_{inj} = 5$ ml/hr where the difference in velocity front is about 20%. As the flow rate injected decreases, the difference between the velocities of the horizontal/vertical dissolution front increases (Table 2). In fact, in horizontal configuration, the dissolution occurs mostly forward to the tip, in the direction of the flow. Under vertical configuration, however, the dissolution develops both forward to the tip and on the wormhole lateral sides leading to the observed roughness. Under the flow rate of 0.1 ml/hr, the dissolution is widely spread over the whole cross section of the cell, corresponding to the “compact regime” (Figure 10).

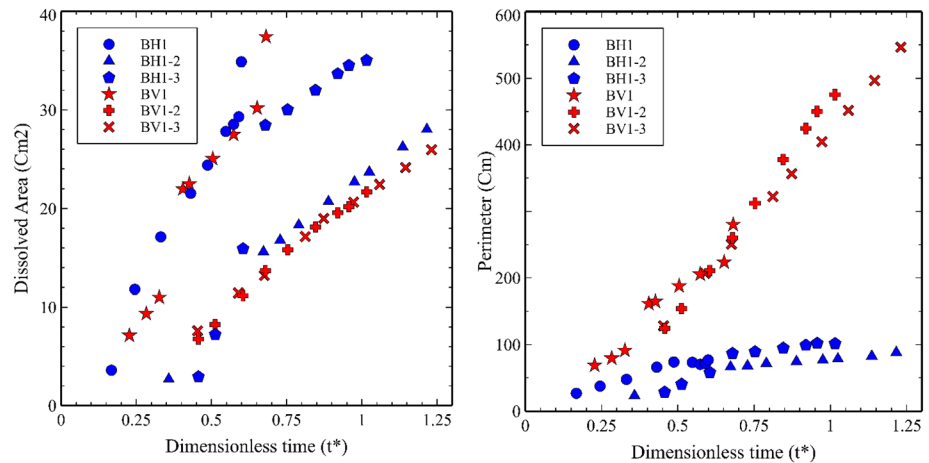


Figure 11. Evolution of interface between dissolved and nondissolved area (or perimeter) (left) and dissolved area (right) against dimensionless time at 1 ml/hr for both configurations.

These comments are fully consistent with the evolution of the PVBT (Figure 3) where the vertical configuration (low mean front velocity) is found above the horizontal configuration. However, the more the injected flow rate decreases, the more the values of certain parameters used in our analysis vary. This variation could lead us to a certain reserve concerning the reproducibility of the experiments. Indeed, if we take into account the experiments carried out for $Q_{inj} = 1$ ml/hr we observe that the PVBT values for the vertical configuration vary between 3.46 to 9.58 with a standard deviation about 3.1, while for the horizontal configuration the same values vary between 2.28 and 8.5 with a standard deviation of about 4.4. If for the vertical configuration this difference could be attributed to instabilities induced by both dissolution and density contrast resulting in nonreproducible configurations, for the horizontal configuration this difference could only be attributed to instabilities induced by the dissolution. This result signifies that at low injection rates the slightest local variation in permeability and/or porosity can lead to a large variation in breakthrough time although the dissolution regime remains unchanged. An experiment in vertical configuration could thus have a breakthrough time greater than an experiment in horizontal configuration. This high variability is specific to the conical regime. At higher flow rate, the system is dominated by convection and therefore the flow will tend to focus in one unique wormhole. At very low flow rate, the dissolution front is driven by diffusion which kills the instabilities induced by dissolution and is more stable. The 1 ml/hr corresponds to an intermediate case where neither convection nor diffusion prevails and permeability heterogeneities drive dissolution. As a consequence, multiple wormholes can develop significantly, hence causing a large error bar (mostly relating to how many wormholes were developed).

A similar observation than for the conical regime concerning the fluid-solid interface roughness can be made (Figure 10), albeit with the vertical configurations surface to perimeter ratios being significantly smaller than the horizontal one (Table 2). Despite the variability of the compacity parameter, there is a clear discrepancy between horizontal and vertical values with no overlapping of the range of values.

In order to further investigate the roughness, let us focus our attention on the one of the injected flow rate discussed above, that is, $Q_{inj} = 1$ ml/hr via the evolution of the estimated perimeter at the geometrical interface between the dissolved zone and the partially dissolved zone and the dissolved surface with dimensionless time (Figure 11). As shown in Figure 11, left, it results that for a given quantity of pure water injected, and therefore for a given time, the dissolved surface (i.e., the dissolved mass) shows two distinct “trends” regardless of considered configuration. Thus, the experiments noted by BH1_2 are grouped together with BV1_2 and BV1_3 while BH1_1 presents values close to BV1_1 (BH = horizontal configuration, BV = vertical configuration, _1 = the index of the experiment). As for BH1_3, it covers both “trends.” At the beginning of the experiment, its dynamics rather follows that of the first grouping, while at the end of the experiment it is relatively close to the second one. This difference in behavior is certainly due to what can be called an “experimental artifact” translated by the appearance, close to the lateral edge of the cell, of an additional wormhole (Figure 12). This observation is also present on the PVBT curve, with BV1_3,

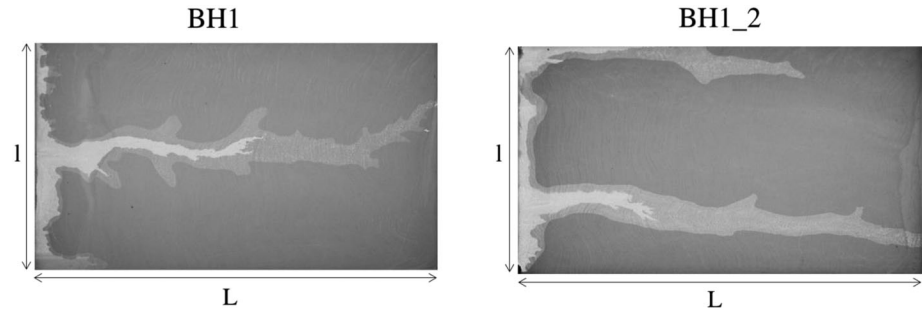


Figure 12. Dissolution pattern for (left) BH1 (without lateral wormhole) and (right) BH1_2 (with lateral wormhole).

BH1_2, and BV1_2 being the higher values and BH1, BV1, and BH1_3 the lower values. On the other hand, the geometrical interface area (or perimeter – Figure 11, right), which can be assimilated to a reactive interface, demonstrate a clear separation between vertical and horizontal configurations with the former being clearly greater than the latter. This difference reinforces our experimental observation concerning the development of roughness in the vertical configuration. Besides, it should be noted that the variability is significantly lower for the perimeter than for the dissolved surface.

Considering the development of interface roughness as a clear discrepancy between vertical and horizontal configuration, it is very likely the consequence of buoyancy-driven instabilities. Indeed, the high Richardson number of the conical and compact regimes (10^5 – 10^7) suggests that, in vertical configuration, the free convection becomes preponderant and this behavior can be assimilated with the one described for supercritical CO_2 storage in brine aquifers (Babaei & Islam, 2018; Fu et al., 2015; Sainz-Garcia et al., 2017) for which the formation of convective cells was found numerically. In essence, since the injection velocity is very low, our configuration is reminiscent of the Rayleigh-Benard-Darcy type problem. Classically, a critical solutal Rayleigh number $Ra_c = \frac{\Delta\rho g l^3}{\mu D}$ with μ the fluid dynamic viscosity (Pa s) and l a characteristic length (m), is used to identify the onset of convection instability, but this value may vary significantly depending on boundary conditions and geometry. Since our boundary conditions are potentially time variable, it is not fully equivalent to the classical Rayleigh-Bénard problem and it is more appealing to make a parallel with the behavior of a salt block immersed in water investigated by Philippi et al. (2019) in which an estimate of Ra_c between 600 and 1,300 (due to the uncertainty on the boundary layer thickness l) is found. Based on this study also, the dissolved flux should tend toward a constant value which can be related to the experimental Rayleigh number Ra via the following relationship:

$$F = (Ra)^{-1/3} C_m \left(\frac{D g \Delta\rho^{\text{eff}}}{\mu} \right)^{1/3}$$

In the vertical configuration, a quasi-steady dissolved flux is also observed (see Figure 11) which supports the comparison with the study of Philippi et al. (2019). Using a similar approach with that proposed by

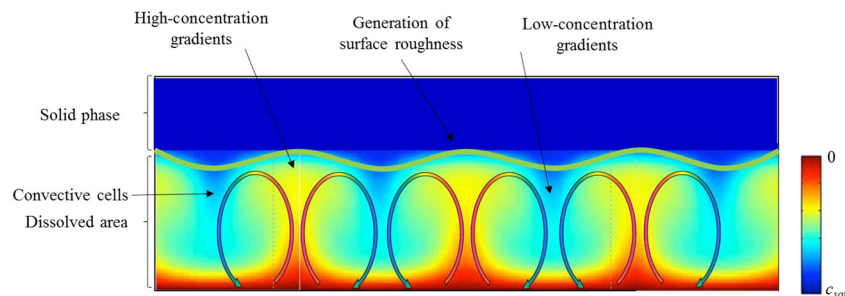


Figure 13. Conceptual description of the interface roughness generation.

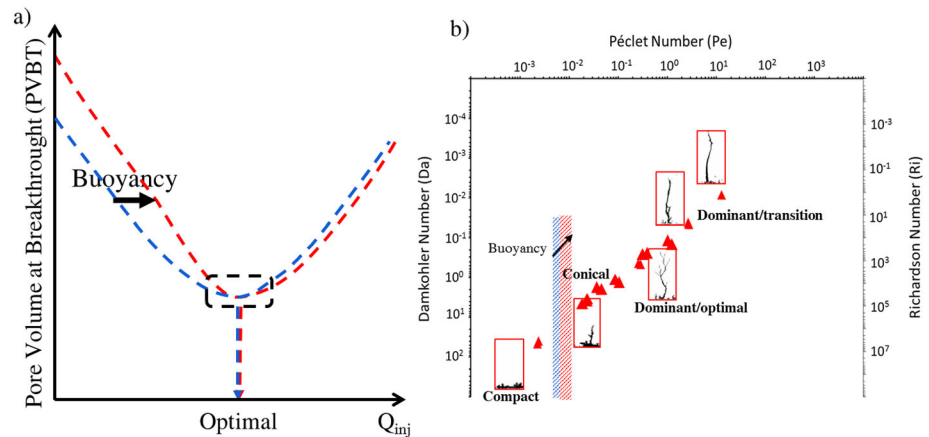


Figure 14. Impact of buoyancy (black arrows) on the PVBT curves (a) and on the transition between dissolution patterns as illustrated on the regime diagram (b). Data points and images correspond to the results in vertical configuration.

Slim et al. (2013), the dissolution mass flux per unit area (defined in our case by $A = e \times (l - 2 \times f)$) for each experiment can be determined as $F = (dM/dt)/A$, where M is the dissolved mass estimated through the dissolved areas. We obtain dissolved fluxes which vary between $6.0 \times 10^{-5} \text{ kg/m}^2 \text{ s}$ for $Q_{inj} = 0.1 \text{ ml/hr}$ and $3.0 \times 10^{-4} \text{ kg/m}^2 \text{ s}$ for $Q_{inj} = 2 \text{ ml/hr}$. For these dissolved fluxes, Ra values are relatively large ($>10^4$), in any case, much higher than the critical value proposed by Philippi et al. (2019) corresponding to the onset of instabilities. If we extend this analysis for the higher flow rates, the experimental values of Rayleigh number fall below Ra_c for flow rates between 5 and 10 ml/hr which is consistent with our previous observations.

Therefore, we may suppose that the injected fluid causes the appearance and development of gravitational instabilities resulting in concentration finger-like structures of different amplitudes that migrate upward. In the compact regime, where the dissolution is spread over the whole width of the domain, these convective cells transport the high-concentration solution, that is, salt-saturated water, toward the injection surface and, conversely, the injected fresh water toward the dissolution front. As a result, a mixing zone develops with perturbations in concentration located at the dissolved/undissolved zone interface. These concentration instabilities drive the observed surface roughness as illustrated conceptually in (Figure 13). And the higher Ra is, the higher is the surface roughness. In the conical regime, a similar phenomenon could be envisioned, though localized in the inner wormhole and causing the increased roughness and lateral extension.

4. Conclusions

In the present work, experimental results of the dissolution of a salt plaster material considering two configurations (vertical and horizontal) and multiple flow rates were discussed with the aim to evaluate the impact of density driven flow on dissolution patterns. The following results were obtained:

- i. In contrast to the changes generated by the density contrast in the dissolution patterns of a vertical fracture (Oltéan et al., 2013), the overall dissolution regimes were preserved independently of the cell orientation and no other regime was obtained. These regimes may be summarized in a diagram following the work of Golfier et al. (2002) (Figure 14b).
- ii. Although the PVBT curves show a classic behavior with an optimal value closed to the dominant/optimal regime, they are not superimposed especially for the low flow rates. Therefore, the PVBT for the vertical configuration is seemingly shifted upward compared to the horizontal configuration suggesting that, for high Richardson numbers, the forward velocity of the dissolution front is slowed down by the density contrast (Figure 14a). This unexpected behavior was explained by using the morphological parameters of the dissolved zone (surface, perimeter, roughness, and tortuosity) derived from a careful interpretation of the experimental images. Therefore, in the compact and conical regimes, the buoyancy effects interpreted through the apparition and the development of the convective cells and/or chaotic mixture lead to an increase in the roughness at the interface between dissolved/undissolved or

dissolved/partially dissolved zones (Figure 14a). Note that, for intermediate and low Richardson numbers, both PVBT curves are converging toward one another which means that from the dominant/optimal pattern the influence of the density contrast is negligible (Figure 14b).

On top of these remarks, another phenomenon was observed in link with the nature of the medium used; the salt-plaster mixture likely causes the apparition of two different dissolution zones (one partial and one total) especially developed in the conical regime. The hypothesis used to explain such an observation has been linked to the differences in solubility between plaster and salt.

In order to further precise the regimes' transitions as well as to evaluate our proposed physical explanation, a numerical study would be necessary. Numerical study allows the testing of a wide range of parameters and/or couplings not always easily available experimentally. However, it should be noted that simulating instability propagation under high reaction rate and buoyancy coupling remains complex and is a highly challenging goal for future works.

Data Availability Statement

The data presented in this manuscript are provided through Figshare (https://figshare.com/projects/Experimental_insights_into_the_interplay_between_buoyancy_convection_and_dissolution_reaction/76041).

Acknowledgments

This work has been partially supported by the French National Research Agency through the national program "Investissements d'avenir" with the reference ANR-10-LABX-21-10/LABEX RESSOURCES21, the ICEEL Carnot Institute (grant MultiEcHydro) and the LUE Mirabelle + 3-D Soil Test project.

References

- Babaei, M., & Islam, A. (2018). Convective-reactive CO₂ dissolution in aquifers with mass transfer with immobile water. *Water Resources Research*, 54, 9585–9604. <https://doi.org/10.1029/2018WR023150>
- Bazin, B. (2000). From matrix acidizing to acid fracturing: A laboratory evaluation of acid/rock interactions. *SPE Production & Facilities*, 15(4), 1–8. <https://doi.org/10.2118/66566-pa>
- Bear, J. (1972). *Dynamics of fluids in porous media*. New York: Elsevier.
- Campana, C., & Fidelibus, M. D. (2015). Reactive-transport modelling of gypsum dissolution in a coastal karst aquifer in Puglia, southern Italy. *Hydrogeology Journal*, 23(7), 1381–1398. <https://doi.org/10.1007/s10040-015-1290-x>
- Chaudhuri, A., Rajaram, H., Viswanathan, H., Zvyoloslki, G., & Stauffer, P. (2009). Buoyant convection resulting from dissolution and permeability growth in vertical limestone fractures: Buoyant convection from aperture growth. *Geophysical Research Letters*, 36, L03401. <https://doi.org/10.1029/2008GL036533>
- Chen, Y., Ma, G., Li, T., Wang, Y., & Ren, F. (2018). Simulation of wormhole propagation in fractured carbonate rocks with unified pipe-network method. *Computers and Geotechnics*, 98, 58–68. <https://doi.org/10.1016/j.compgeo.2017.11.009>
- Cohen, C. E., Ding, D., Quintard, M., & Bazin, B. (2008). From pore scale to wellbore scale: Impact of geometry on wormhole growth in carbonate acidization. *Chemical Engineering Science*, 63(12), 3088–3099. <https://doi.org/10.1016/j.ces.2008.03.021>
- Colombani, J. (2008). Measurement of the pure dissolution rate constant of a mineral in water. *Geochimica et Cosmochimica Acta*, 72(23), 5634–5640. <https://doi.org/10.1016/j.gca.2008.09.007>
- Daccord, G. (1987). Chemical dissolution of a porous medium by a reactive fluid. *Physical Review Letters*, 58(5), 479–482. <https://doi.org/10.1103/PhysRevLett.58.479>
- Dijk, P. E., Berkowitz, B., & Yechieli, Y. (2002). Measurement and analysis of dissolution patterns in rock fractures: Measurement and analysis of dissolution in rock fractures. *Water Resources Research*, 38(2). <https://doi.org/10.1029/2001WR000246>
- Dutka, F., Starchenko, V., Osselin, F., Magni, S., Szymczak, P., & Ladd, A. J. C. (2020). Time-dependent shapes of a dissolving mineral grain: Comparisons of simulations with microfluidic experiments. *Chemical Geology*, 119459. <https://doi.org/10.1016/j.chemgeo.2019.119459>
- Emami-Meybodi, H., Hassanzadeh, H., Green, C. P., & Ennis-King, J. (2015). Convective dissolution of CO₂ in saline aquifers: Progress in modeling and experiments. *International Journal of Greenhouse Gas Control*, 40, 238–266. <https://doi.org/10.1016/j.ijggc.2015.04.003>
- Fredd, C. N., & Fogler, H. (1998a). The kinetics of calcite dissolution in acetic acid solutions. *Chemical Engineering Science*, 53(22), 3863–3874. [https://doi.org/10.1016/S0009-2509\(98\)00192-4](https://doi.org/10.1016/S0009-2509(98)00192-4)
- Fredd, C. N., & Fogler, H. S. (1998b). Influence of transport and reaction on wormhole formation in porous media. *AIChE Journal*, 44(9), 1933–1949. <https://doi.org/10.1002/aic.690440902>
- Fredd, C. N., & Miller, M. J. (2000). *Validation of carbonate matrix stimulation models* (pp. 1–14). Paper presented at SPE International Symposium on Formation Damage Control, Society of Petroleum Engineers, Lafayette, LA. <https://doi.org/10.2118/58713-MS>
- Fu, X., Cueto-Felgueroso, L., Bolster, D., & Juanes, R. (2015). Rock dissolution patterns and geochemical shutdown of CO₂-brine-carbonate reactions during convective mixing in porous media. *Journal of Fluid Mechanics*, 764, 296–315. <https://doi.org/10.1017/jfm.2014.647>
- Golfier, F., Zarcone, C., Bazin, B., Lenormand, R., Lasseux, D., & Quintard, M. (2002). On the ability of a Darcy-scale model to capture wormhole formation during the dissolution of a porous medium. *Journal of Fluid Mechanics*, 457, 213–254. <https://doi.org/10.1017/S0022112002007735>
- Gray, F., Anabaraonye, B., Shah, S., Boek, E., & Crawshaw, J. (2018). Chemical mechanisms of dissolution of calcite by HCl in porous media: Simulations and experiment. *Advances in Water Resources*, 121, 369–387. <https://doi.org/10.1016/j.advwatres.2018.09.007>
- Guo, J., Laouafa, F., & Quintard, M. (2016). A theoretical and numerical framework for modeling gypsum cavity dissolution. *International Journal for Numerical and Analytical Methods in Geomechanics*, 40(12), 1662–1689. <https://doi.org/10.1002/nag.2504>
- Hidalgo, J. J., MacMinn, C. W., & Juanes, R. (2013). Dynamics of convective dissolution from a migrating current of carbon dioxide. *Advances in Water Resources*, 62, 511–519. <https://doi.org/10.1016/j.advwatres.2013.06.013>

- Hoefner, M. L., & Fogler, H. S. (1988). Pore evolution and channel formation during flow and reaction in porous media. *AICHE Journal*, 34(1), 45–54. <https://doi.org/10.1002/aic.690340107>
- Izgec, O., Zhu, D., & Hill, A. D. (2010). Numerical and experimental investigation of acid wormholing during acidization of vuggy carbonate rocks. *Journal of Petroleum Science and Engineering*, 74(1–2), 51–66. <https://doi.org/10.1016/j.petrol.2010.08.006>
- Johnson, K. S. (2005). Subsidence hazards due to evaporite dissolution in the United States. *Environmental Geology*, 48(3), 395–409. <https://doi.org/10.1007/s00254-005-1283-5>
- Johnson, K. S. (2008). Evaporite-karst problems and studies in the USA. *Environmental Geology*, 53(5), 937–943. <https://doi.org/10.1007/s00254-007-0716-8>
- Kang, Q., Lichtner, P. C., & Zhang, D. (2007). An improved lattice Boltzmann model for multicomponent reactive transport in porous media at the pore scale: Multicomponent reactive transport. *Water Resources Research*, 43, W12S14. <https://doi.org/10.1029/2006WR005551>
- Lehmann, G., & Legland, D. (2012). *Efficient N-dimensional surface estimation using Crofton formula and run-length encoding* (p. 11). Retrieved from <https://hal.inrae.fr/hal-02811118/document>
- Liang, C., Cui, M., Xue, H., Zou, H., Jiang, W., & Liu, P. (2015). *Simulation and analysis of wormhole structure affected by mineralogy heterogeneity in carbonate rocks* (Vol. 20, p. 21). Retrieved from https://www.researchgate.net/publication/296884266_Simulation_and_analysis_of_wormhole_structure_affected_by_mineralogy_heterogeneity_in_carbonate_rocks
- Liu, M., Shabaninejad, M., & Mostaghimi, P. (2017). Impact of mineralogical heterogeneity on reactive transport modelling. *Computers & Geosciences*, 104, 12–19. <https://doi.org/10.1016/j.cageo.2017.03.020>
- Luo, H., Quintard, M., Debenest, G., & Laouafa, F. (2012). Properties of a diffuse interface model based on a porous medium theory for solid–liquid dissolution problems. *Computational Geosciences*, 16(4), 913–932. <https://doi.org/10.1007/s10596-012-9295-1>
- Luquot, L., Hebert, V., & Rodriguez, O. (2016). Calculating structural and geometrical parameters by laboratory measurements and X-ray microtomography: A comparative study applied to a limestone sample before and after a dissolution experiment. *Solid Earth*, 7(2), 441–456. <https://doi.org/10.5194/se-7-441-2016>
- Mayer, K. U., Frind, E. O., & Blowes, D. W. (2002). Multicomponent reactive transport modeling in variably saturated porous media using a generalized formulation for kinetically controlled reactions. *Water Resources Research*, 38(9), 1174. <https://doi.org/10.1029/2001WR000862>
- Menke, H. P., Bijeljic, B., Andrew, M. G., & Blunt, M. J. (2015). Dynamic three-dimensional pore-scale imaging of reaction in a carbonate at reservoir conditions. *Environmental Science & Technology*, 49(7), 4407–4414. <https://doi.org/10.1021/es505789f>
- Menke, H. P., Reynolds, C. A., Andrew, M. G., Pereira Nunes, J. P., Bijeljic, B., & Blunt, M. J. (2018). 4D multi-scale imaging of reactive flow in carbonates: Assessing the impact of heterogeneity on dissolution regimes using streamlines at multiple length scales. *Chemical Geology*, 481, 27–37. <https://doi.org/10.1016/j.chemgeo.2018.01.016>
- Min, T., Gao, Y., Chen, L., Kang, Q., & Tao, W. (2016). Changes in porosity, permeability and surface area during rock dissolution: Effects of mineralogical heterogeneity. *International Journal of Heat and Mass Transfer*, 103, 900–913. <https://doi.org/10.1016/j.ijheatmasstransfer.2016.07.043>
- Oltéan, C., Golfier, F., & Buès, M. A. (2013). Numerical and experimental investigation of buoyancy-driven dissolution in vertical fracture. *Journal of Geophysical Research: Solid Earth*, 118, 2038–2048. <https://doi.org/10.1002/jgrb.50188>
- Ott, H., & Oedai, S. (2015). Wormhole formation and compact dissolution in single- and two-phase CO₂-brine injections. *Geophysical Research Letters*, 42, 2270–2276. <https://doi.org/10.1002/2015GL063582>
- Panga, M. K. R., Ziauddin, M., & Balakotaiah, V. (2005). Two-scale continuum model for simulation of wormholes in carbonate acidization. *AICHE Journal*, 51(12), 3231–3248. <https://doi.org/10.1002/aic.10574>
- Philippi, J., Berhanu, M., Derr, J., & Courrech du Pont, S. (2019). Solutal convection induced by dissolution. *Physical Review Fluids*, 4(10), 103801. <https://doi.org/10.1103/PhysRevFluids.4.103801>
- Raines, M. A., & Dewers, T. A. (1997). Mixed transport/reaction control of gypsum dissolution kinetics in aqueous solutions and initiation of gypsum karst. *Chemical Geology*, 140, 29–48. [https://doi.org/10.1016/S0009-2541\(97\)00018-1](https://doi.org/10.1016/S0009-2541(97)00018-1)
- Sainz-Garcia, A., Abarca, E., Nardi, A., Grandia, F., & Oelkers, E. H. (2017). Convective mixing fingers and chemistry interaction in carbon storage. *International Journal of Greenhouse Gas Control*, 58, 52–61. <https://doi.org/10.1016/j.ijggc.2016.12.005>
- Schechter, R. S., & Gidley, J. L. (1969). The change in pore size distribution from surface reactions in porous media. *AICHE Journal*, 15(3), 339–350. <https://doi.org/10.1002/aic.690150309>
- Slim, A. C., Bandi, M. M., Miller, J. C., & Mahadevan, L. (2013). Dissolution-driven convection in a Hele–Shaw cell. *Physics of Fluids*, 25(2), 024101. <https://doi.org/10.1063/1.4790511>
- Snippe, J., Berg, S., Ganga, K., Brussee, N., & Gdanski, R. (2020). Experimental and numerical investigation of wormholing during CO₂ storage and water alternating gas injection. *International Journal of Greenhouse Gas Control*, 94, 102901. <https://doi.org/10.1016/j.ijggc.2019.102901>
- Snippe, J., Gdanski, R., & Ott, H. (2017). Multiphase modelling of wormhole formation in carbonates by the injection of CO₂. *Energy Procedia*, 114, 2972–2984. <https://doi.org/10.1016/j.egypro.2017.03.1426>
- Soulaine, C., Roman, S., Kovscek, A., & Tchelepi, H. A. (2017). Mineral dissolution and wormholing from a pore-scale perspective. *Journal of Fluid Mechanics*, 827. <https://doi.org/10.1017/jfm.2017.499>
- Szymczak, P., & Ladd, A. J. C. (2004). Microscopic simulations of fracture dissolution. *Geophysical Research Letters*, 31, L23606. <https://doi.org/10.1029/2004GL021297>
- Szymczak, P., & Ladd, A. J. C. (2011). Instabilities in the dissolution of a porous matrix: Dissolutional instabilities. *Geophysical Research Letters*, 38, L07403. <https://doi.org/10.1029/2011GL046720>
- Weisbrod, N., Alon-Mordish, C., Konen, E., & Yechieli, Y. (2012). Dynamic dissolution of halite rock during flow of diluted saline solutions: Dynamic dissolution of salt rock. *Geophysical Research Letters*, 39, L09404. <https://doi.org/10.1029/2012GL051306>